J. Fluid Mech. (2024), *vol*. 997, A53, doi:10.1017/jfm.2024.818

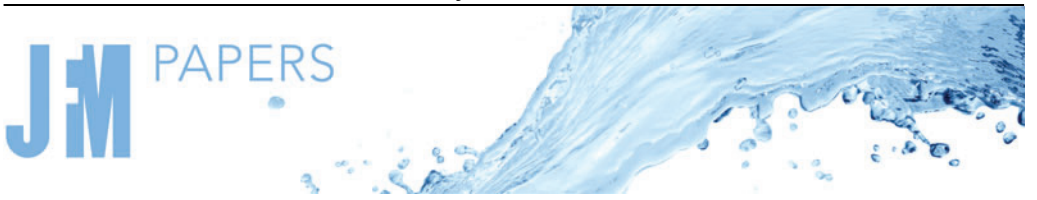

Two-point statistics in non-homogeneous rotating turbulence

P. Beaumard[1], **P. Bragança**[1], **C. Cuvier**[1] **and J.C. Vassilicos**[1],†

[1]Univ. Lille, CNRS, ONERA, Arts et Metiers Institute of Technology, Centrale Lille, UMR 9014 – LMFL – Laboratoire de Mécanique des Fluides de Lille, Kampé de Fériet, F-59000 Lille, France

(Received 29 March 2024; revised 17 July 2024; accepted 24 August 2024)

Time-resolved two-dimensional two-component particle image velocimetry measurements with high spatial resolution are carried out in a water tank agitated by four blades rotating at constant speed. Different blade geometries and rotation speeds are tested for the purpose of modifying turbulent flow conditions. In all cases where no baffles are used to break the rotation, the Zeman length is an order of magnitude smaller than the Taylor length. Compared with the cases with baffles which break the rotation, in the unbaffled cases turbulence production and/or mean advection are significant and the turbulence nonlinearity is dramatically reduced for the horizontal (i.e. normal to the axis of rotation) two-point turbulence fluctuating velocities. This nonlinearity reduction is manifest not only in the interscale turbulent energy transfer but also in the interspace turbulent energy transfer, which nearly vanishes. However, the nonlinearity is not reduced for the vertical two-point turbulence fluctuating velocities: the corresponding interscale turbulent transfer rate is in fact intensified, and its dependence on the two-point separation distance, as well as that of the corresponding interspace turbulent transfer rate, which does not vanish, is significantly modified. Even though non-homogeneities are very different for different blades and rotation speeds in the unbaffled cases, the horizontal fluctuating velocity's second-order structure function collapses with scalings which resemble predictions for homogeneous turbulence subject to strong rotation. The vertical fluctuating velocity's second-order structure function does not collapse for different blade geometries by neither these nor the Kolmogorov predictions.

Key words: rotating turbulence, turbulence theory

1. Introduction

Rotating turbulent flows are present in many natural and industrial contexts, including cyclones, tornadoes, industrial mixers and rotor wakes, to name but a few. The turbulence

† Email address for correspondence: john-christos.vassilicos@centralelille.fr

in these flows is typically non-homogeneous so that the Kolmogorov theory of equilibrium cascades (see Kolmogorov 1941*a*,*b*; Batchelor 1953; Frisch 1995; Sagaut & Cambon 2018; Chen & Vassilicos 2022; Galtier 2022) may not apply to them on either or both accounts of absence of homogeneity and presence of rotation (see Sagaut & Cambon (2018) and Galtier (2022) for rotating homogeneous turbulence).

Under assumptions of local equilibrium (local homogeneity and stationarity of turbulence) and two similarity hypotheses, the Kolmogorov theory implies that the energy spectrum $E(k)$ scales with the turbulence dissipation rate ε as $E(k) \sim \varepsilon^{2/3}k^{-5/3}$ in an inertial range of wavenumbers k (Obukhov 1941; Batchelor 1953; Frisch 1995). However, when the homogeneous turbulence is subjected to rotation with constant angular velocity Ω, one expects a depletion of nonlinearity when the rotation time scale Ω^{-1} is much smaller than the turbulence time scale $\sqrt{K}/L$, i.e. $Ro^L \equiv \sqrt{K}/(\Omega L) \ll 1$, where K is the turbulence kinetic energy and L is an integral length scale (see Sagaut & Cambon 2018; Galtier 2022). Furthermore, wavenumbers k for which Ω^{-1} is smaller than the local turbulence time scale $(\varepsilon k^2)^{-1/3}$ are expected to be significantly affected by the rotation so that the energy spectrum's scaling changes to

$$E(k) \sim \sqrt{\epsilon\Omega}k^{-2} \tag{1.1}$$

for $k \ll l_\Omega^{-1}$, where

$$l_\Omega^{-1} \equiv \sqrt{\Omega^3/\varepsilon}, \tag{1.2}$$

as has been claimed for both stationary (e.g. Zhou 1995; Canuto & Dubovikov 1997) and decaying (Zeman 1994; Canuto & Dubovikov 1997) homogeneous turbulence. (The length scale l_Ω is sometimes referred to as the Zeman length and serves to identify the length scales larger than l_Ω where energy accumulates towards the plane normal to the rotation axis; see Delache, Cambon & Godeferd (2014).) A Rossby number Ro^L much smaller than 1 is equivalent to $l_\Omega \ll L$; see for example Canuto & Dubovikov (1997), which also introduced the parameter $N \equiv K/(\nu\Omega)$ to discriminate between complete suppression of nonlinear energy transfer ($N < 1$) and depletion without complete suppression of nonlinear energy transfer ($N > 1$).

Some support for (1.1) has been provided by direct numerical simulations of non-decaying rotating periodic turbulence forced at the large scales in the work of Yeung & Zhou (1998). Experiments in decaying grid-generated (i.e. nominally homogeneous) rotating turbulence by Morize, Moisy & Rabaud (2005) have returned spectra $E(k) \sim k^{-n(t)}$ with time-dependent exponents $n(t)$ that vary from approximately $5/3$ to approximately 2.3 as the time-dependent Rossby number decreases below 1 during decay. However, in a laboratory experiment of quasi-two-dimensional turbulent flow in a rapidly rotating annulus, Baroud *et al.* (2002) reported a second-order structure function that is proportional to the distance between the two points defining the structure function, in agreement with a k^{-2} spectrum, but they did not check whether the structure function was proportional to $\sqrt{\epsilon\Omega}$ as per (1.1). Such a check would matter because k^{-2} spectra with different prefactors have also been proposed, such as $E(k) \sim \delta S^{-1}k^{-2}$ for non-local helicity cascades in homogeneous turbulence, where δ is a constant helicity transfer rate and S is a large-scale shear rate (see Nazarenko & Laval 2000; Herbert *et al.* 2012).

Most theoretical works on rotating turbulence have been concerned with homogeneous turbulence (see Galtier 2009; Sagaut & Cambon 2018; Galtier 2022), examples of theoretical prediction for rotating homogeneous turbulence being (1.1) and depletion of nonlinearity. In particular, wave turbulence theory, which describes rapidly rotating

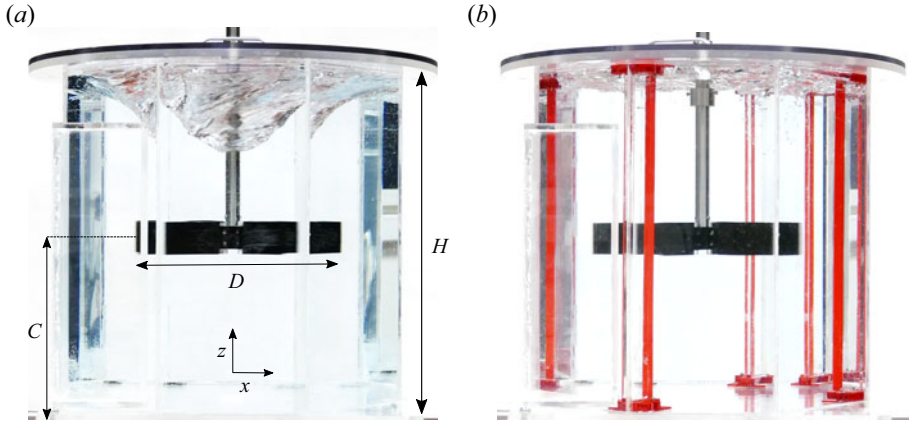

Figure 1. Mixing tank: (*a*) without baffles; (*b*) with baffles.

turbulence with very small Rossby numbers (see Godeferd & Moisy 2015; Sagaut & Cambon 2018; Galtier 2022), assumes statistical homogeneity. However, the turbulence in the rotating annulus of Baroud *et al.* (2002) was probably not homogeneous and a scaling with some indirect agreement with (1.1) was nevertheless found in this flow. The question arises as to whether well-defined scalings and laws exist for non-homogeneous rotating turbulence and how they compare with their analogues in homogeneous rotating turbulence. This is a definite step beyond current theoretical limits.

To address this question, and also to assess whether and how rotation affects nonlinearity, we use an unsophisticated and rather common flow configuration where turbulence is both non-homogeneous and subjected to rotation: a mixer tank where the flow is driven by a rotating impeller. We address the question experimentally with particle image velocimetry (PIV) measurements of the turbulent flow in a region under the impellers. We repeat the experiments with different rotation frequencies and/or different impeller blades and obtain measurements for a wide range of turbulence dissipation rates so as to be able to test scalings similar to those of (1.1).

This paper is structured as follows. First, we describe the PIV experiments in § 2. Then, we assess mean flow non-homogeneity and rotation effects in terms of the Corrsin and Zeman lengths in § 3. Second-order structure functions are analysed in § 4, and we quantify turbulence non-homogeneity as well as nonlinear turbulent energy transfers across scales and across space in § 5 on the basis of a Kármán–Howarth–Monin–Hill (KHMH) two-point energy equation. We draw some conclusions in § 6.

2. Experimental measurements

The experimental set-up and measurement technique are identical to those of Beaumard *et al.* (2024) and associated supplementary material where they are presented in detail. In this section we summarise the main features.

Experiments are carried out with water in the same octagonal acrylic tank originally used by Steiros *et al.* (2017*a*,*b*). The impeller has a radial four-bladed flat-blade turbine, mounted on a stainless steel shaft at the mid-height of the tank; see figure 1(*a*) where the mixer dimensions are also presented: D_T is the tank diameter (45 cm), H is the tank height ($H = D_T$), C is the rotor height ($H/2$) and D is the rotor diameter (about $D_T/2$). Beaumard *et al.* (2024) focused on the turbulence in the baffled tank (four vertical bars on the sides of

	F (Hz)	$\langle\overline{\epsilon'}\rangle$ (m^2 s^{-3})	η (m)	λ (m)	Re_λ
Rectangular blades	2	6.0×10^{-4}	2.0×10^{-4}	6.6×10^{-3}	4.1×10^{2}
Rectangular blades	3	2.1×10^{-3}	1.4×10^{-4}	5.3×10^{-3}	5.2×10^{2}
Fractal blades	2	1.3×10^{-3}	1.6×10^{-4}	5.8×10^{-3}	4.6×10^{2}
Fractal blades	2.5	2.3×10^{-3}	1.5×10^{-4}	5.5×10^{-3}	5.3×10^{2}
Rectangular blades with baffles	1	3.6×10^{-3}	1.1×10^{-4}	4.1×10^{-3}	5.1×10^{2}
Rectangular blades with baffles	1.5	1.2×10^{-2}	8.8×10^{-5}	3.7×10^{-3}	6.5×10^{2}
Fractal blades with baffles	1	2.4×10^{-3}	1.3×10^{-4}	4.9×10^{-3}	4.8×10^{2}
Fractal blades with baffles	1.5	8.2×10^{-3}	1.0×10^{-4}	4.1×10^{-3}	5.8×10^{2}

Table 1. Main turbulence parameters.

the tank; see figure 1*b*) because well-designed baffles break the rotation (baffles of width around $0.12D_T$ designed following Nagata (1975) for close to fully baffled conditions which maximise power consumption and minimise rotation). Here we concentrate on the unbaffled tank (see figure 1*a*) and use results from the baffled tank only for comparison.

To test the robustness of our results and identify scalings, we run experiments with two different types of blade geometry which stimulate the turbulence differently: rectangular blades of 44 mm $\times$ 99 mm size and fractal-like/multiscale blades of the exact same frontal area but much longer perimeter (see more details in Beaumard *et al.* (2024)). This change affects significantly the turbulence properties as the turbulence dissipation rate varies by a factor of 2 at iso-rotation speed in the absence of baffles and by nearly a factor of 4 across the four different unbaffled configurations (different blades, different rotation frequencies F) considered here (see table 1). We use the two-iteration 'fractal2' blade described in Steiros *et al.* (2017*b*). Each of the two types of blade is tested with two different rotor speeds (with and without baffles).

We use two-dimensional two-component (2D2C) PIV in the vertical (x, z) plane (H is along z and D is along x in figure 1*a*). The field of view is aligned with the vertical plane and the impeller's vertical shaft and has its centre offset by 3 ± 1 mm in the y direction (normal to both x and z directions) from the horizontal position of the shaft at the centre of the tank. Its size is 27 mm $\times$ 28 mm and it is placed under the impeller with its centre at a distance of 0.118 m from the bottom of the tank. All details about these experiments are presented in Beaumard *et al.* (2024).

The PIV resolution (interrogation window size) is between 3.4η and 5.1η depending on the configuration, where the Kolmogorov length $\eta \equiv (\nu^3/\langle\overline{\epsilon'}\rangle)^{1/4}$ is calculated by averaging the turbulence dissipation rate ϵ' over the PIV field of view (angular brackets) and over time (overbar). To be precise, ϵ' is the pseudo-dissipation (see Pope 2000) estimated from our 2D2C PIV data using its axisymmetric formulation (see Beaumard *et al.* 2024). Time-resolved measurements were carried out in order to denoise the dissipation from the PIV measurement noise, as explained in the supplementary material of Beaumard *et al.* (2024).

For each configuration, 150 000 velocity fields are recorded in time, including 50 000 fully uncorrelated velocity field samples for convergence. This corresponds to a time interval of around 139 min. Averaging over time is not sufficient for convergence and we therefore also apply averaging over space, which greatly improves it. More details about convergence are available in Beaumard *et al.* (2024).

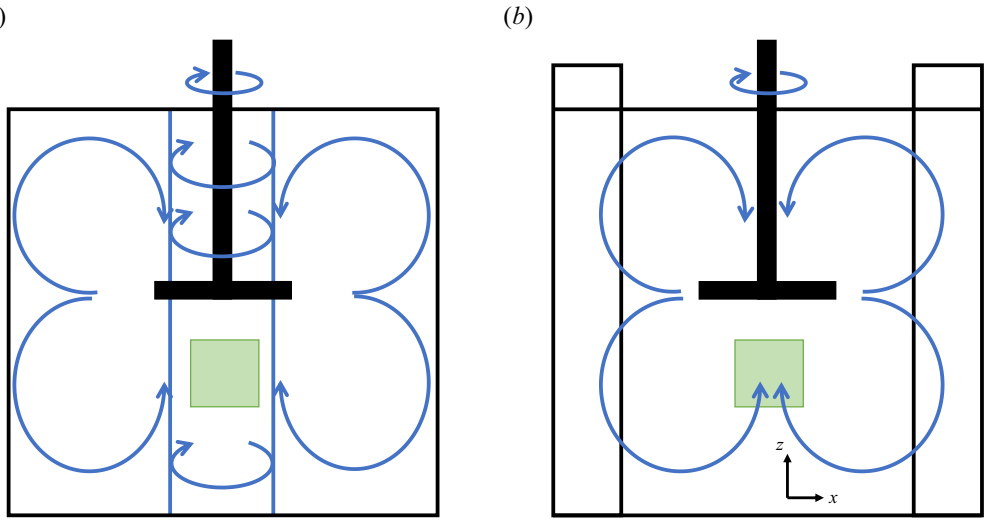

Figure 2. Schematic of mean flow in a mixer with and without baffles (Nagata 1975). The measurement plane is shown as a green square. (*a*) Flow without baffles. (*b*) Flow with baffles.

The rotation frequency F varies between 1 and 3 Hz (see table 1). The Reynolds number is $Re = 2\pi FL^2/\nu$, where $L = R = D/2 \approx 11.25$ cm is an estimate of the rotor radius. The value of Re is large, higher than 8×10^4, and the flow is turbulent. The Rossby number is estimated as $R_O^L = K^{1/2}/(\Omega L)$, where K is estimated as $\langle \overline{u_x'^2} \rangle + \langle \overline{u_z'^2} \rangle$, R is used as an estimate of the integral length scale L of the turbulence and $\Omega = 2\pi F$. Our values of R_O^L are around 0.02 for unbaffled configurations and around 0.06 for baffled configurations. The smaller Rossby number for the unbaffled cases reflects the fact that the rotation affects the turbulence more for these configurations than for the baffled configurations. However, the rotor angular velocity Ω is not representative of the flow rotation in the case of the baffled configurations because the baffles break the flow rotation as explained in Nagata (1975) (see figure 2). Therefore, the Rossby number is severely underestimated for these configurations and the difference between baffled and unbaffled configurations is much greater than the Rossby number values suggest.

The main turbulent parameters are presented in table 1. They include the turbulence dissipation rate $\langle \overline{\epsilon'} \rangle$ and the Kolmogorov and Taylor length scales η and λ, respectively. Details concerning the calculation of the parameters can be found in Beaumard *et al.* (2024).

The Taylor-length-based Reynolds number Re_λ is larger than 410 in all configurations. Values of Re_λ are broadly comparable between all configurations, so no significant Reynolds number effect is expected when comparing one with the other.

In figure 3(*a*), we plot the mean flow velocity for one of our four non-baffled configurations, but the plot is representative of the four configurations. The mean flow velocity is oriented horizontally from right to left and is very small in magnitude. These observations evidence the solid-body rotation identified in Nagata (1975) and shown schematically in figure 2(*a*). The solid-body rotation appears in the measurement domain because of the small measurement offset in the y direction. In figure 3(*b*), we plot the mean flow velocity of one representative baffled configuration. The mean flow velocity is oriented vertically from bottom to top and is significant. This observation is consistent

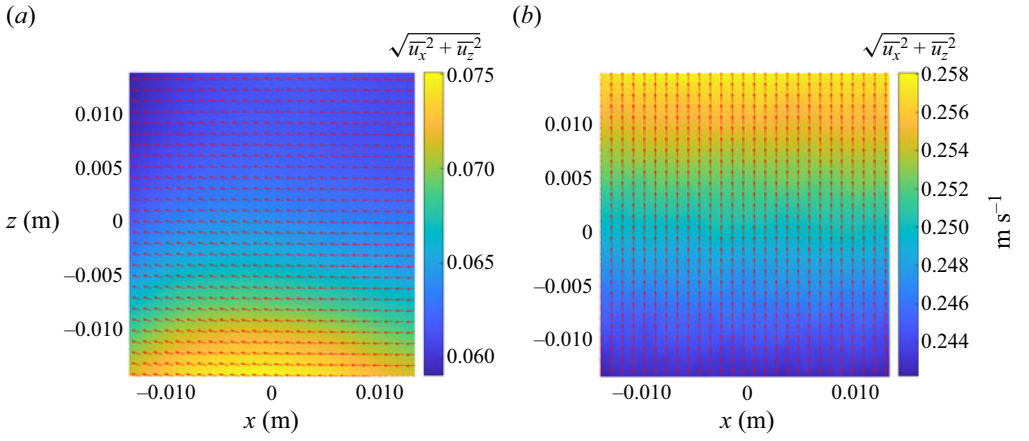

Figure 3. Mean flow measurement within the measurement planes shown in figure 2. (*a*) Rectangular blade without baffles ($F = 3$ Hz). (*b*) Rectangular blade with baffles ($F = 1.5$ Hz).

with absence of rotation in the field of view and with the mean flow structure described in Nagata (1975) and shown in figure 2(*b*).

3. Mean flow non-homogeneity and rotation at small scales

The Corrsin length l_C (Corrsin 1958) was introduced to distinguish between length scales above l_C where mean shear S dominates because its time scale S^{-1} is smaller than the time scale of nonlinear evolution of eddies at such scales and length scales below l_C where the mean flow may be considered locally homogeneous because the nonlinear evolution time scale at such scales is smaller than S^{-1}. The Corrsin length aims to assess mean flow non-homogeneity rather than turbulence non-homogeneity, which we evaluate in § 5.

We define an estimate of the Corrsin length as $\widetilde{l_C} = \langle\overline{\epsilon'}\rangle^{1/2}/\langle S\rangle^{3/2}$, where

$$S = \sqrt{2\left(\frac{\partial\overline{u_x}}{\partial x}\right)^2 + 2\left(\frac{\partial\overline{u_x}}{\partial z}\right)^2 + 2\left(\frac{\partial\overline{u_z}}{\partial x}\right)^2 + \left(\frac{\partial\overline{u_z}}{\partial z}\right)^2}, \tag{3.1}$$

with u_x, u_y and u_z being fluid velocity components in directions x, y and z, respectively. In practice only the mean flow gradients which we can access either directly or via the assumptions $(\partial\overline{u_x}/\partial x)^2 \approx (\partial\overline{u_y}/\partial y)^2$, $(\partial\overline{u_x}/\partial z)^2 \approx (\partial\overline{u_y}/\partial z)^2$ and $(\partial\overline{u_z}/\partial x)^2 \approx (\partial\overline{u_z}/\partial y)^2$ are taken into account. The terms $(\partial\overline{u_x}/\partial y)^2$ and $(\partial\overline{u_y}/\partial x)^2$ are not accessible with our PIV and are therefore not taken into account.

The values of $\widetilde{l_C}$ are presented normalised by λ in table 2; they are much smaller for the unbaffled than for the baffled configurations, suggesting that mean shear non-homogeneity affects much smaller scales in the absence than in the presence of baffles. The actual values of $\widetilde{l_C}$ are between 3λ and 6λ in the unbaffled configurations, even though § 5 suggests that there can be significant turbulence production at scales smaller than that for these configurations. The exact values of the Corrsin length estimates depend on the choice of formula used to calculate S. We should, therefore, be very careful about the interpretation of the actual values of the Corrsin length and focus mainly on its variation between baffled and non-baffled configurations, which should be less dependent on the choice of S. The Corrsin length is a very rough and sometimes misleading indicator (see also Chen &

	F (Hz)	$\widetilde{l_C}/\lambda$	$\widetilde{l_\Omega}/\lambda$	R_O^L	$L/\widetilde{l_\Omega}$	N
Rectangular blades	2	3.5	0.1	0.02	408	297
Rectangular blades	3	5.1	0.1	0.02	397	474
Fractal blades	2	5.2	0.1	0.03	274	493
Fractal blades	2.5	5.5	0.1	0.03	294	581
Rectangular blades with baffles	1	26.4	0.9	0.07	59	1956
Rectangular blades with baffles	1.5	39.5	1.0	0.07	59	2917
Fractal blades with baffles	1	25.8	0.6	0.06	72	1430
Fractal blades with baffles	1.5	38.6	0.8	0.06	72	2083

Table 2. Corrsin length estimate $\widetilde{l_C} = \langle\overline{\epsilon'}\rangle^{1/2}/\langle S\rangle^{3/2}$ with S defined in (3.1), Zeman scale estimate $\widetilde{l_\Omega} = \langle\overline{\epsilon'}\rangle^{1/2}/\Omega^{3/2}$, $R_O^L = K^{1/2}/(\Omega L)$, $L/\widetilde{l_\Omega}$ and $N = K/(\nu\Omega) > 1$, where L is estimated as R and K is estimated as $\langle\overline{u_x'^2}\rangle + \langle\overline{u_z'^2}\rangle$.

Vassilicos 2022) but is nevertheless reliable enough to detect that there is much less mean shear in baffled than in unbaffled flows.

To identify the length scales affected by rotation, we estimate the Zeman length as $\widetilde{l_\Omega} = \langle\overline{\epsilon'}\rangle^{1/2}/\Omega^{3/2}$. The results normalised by λ are presented in table 2. As rotation impacts scales larger than $\widetilde{l_\Omega}$, these results suggest that all scales larger than approximately 0.1λ are affected by rotation in the unbaffled cases.

Our values of $\widetilde{l_\Omega}$ in the baffled cases suggest an impact of rotation at scales larger than in the unbaffled cases but still at relatively small scales. However, the actual values of $\widetilde{l_\Omega}$ for the baffled configurations are misleading as the angular velocity Ω of the rotor is not representative of the actual rotation in the flow, which is negligible because of the baffles. For the baffled configurations, the rotation is therefore expected to affect only scales much larger than our estimate of $\widetilde{l_\Omega}$ in table 2 and is in fact likely to be negligible at all scales.

Table 2 also shows that the Rossby number R_O^L is smaller than 1 (though underestimated in the baffled cases) and that $L/\widetilde{l_\Omega}$ with the integral scale $L \approx R$ is much larger than 1 (though overestimated in the baffled cases) in all configurations and that $N \equiv K/(\nu\Omega)$ is much larger than 1. We might therefore expect a depletion but not a complete suppression of nonlinearity (see § 5) and a non-Kolmogorov scaling in a range of scales larger than $\widetilde{l_\Omega} \approx \lambda/10$ (see § 4) in the unbaffled configurations which are the main subject of this paper.

4. Second-order structure functions

We now compute and analyse second-order structure functions. For this, we introduce the notation $\delta u_i' = (u_i'(\boldsymbol{X}+\boldsymbol{r}) - u_i'(\boldsymbol{X}-\boldsymbol{r}))/2$ where u_i' are the fluctuating velocity components in directions $i = 1, 2, 3$, i.e. directions x, y, z, respectively, $\boldsymbol{X}$ is the centroid and $2\boldsymbol{r}$ is the two-point separation vector. We compute the normalised structure functions $\langle\overline{(\delta u_j')^2}/\sqrt{\overline{\epsilon'}F}\rangle$ for $j = 1$ (velocity fluctuations along the x axis) and $j = 3$ (velocity fluctuations along the z axis) by averaging over time, i.e. over our 150 000 samples (which correspond to 50 000 uncorrelated samples), and also averaging over $\boldsymbol{X}$, i.e. over the planar space of our field of view. The additional averaging over space is necessary for good convergence of our statistics. Note that the structure functions so normalised have dimensions of length.

The normalised structure function $\langle\overline{(\delta u_x')^2}/\sqrt{\overline{\epsilon'}F}\rangle$ is plotted versus r_x and r_z in figure 4(*a*,*b*), respectively, for the four unbaffled configurations. We evaluate the spatial

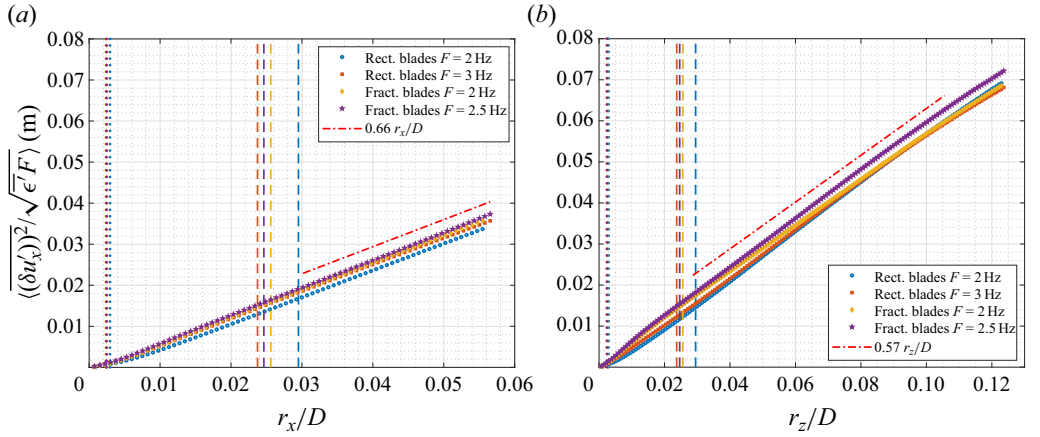

Figure 4. Normalised structure function $\overline{\langle(\delta u_x')^2\rangle}/\sqrt{\overline{\epsilon'}F}\rangle$ space-averaged over the field of view versus (*a*) r_x (for $r_z = 0$) and (*b*) r_z (for $r_x = 0$). The units on the vertical axes are metres (m). The Taylor length scales of the different configurations are plotted as vertical dashed lines and the Zeman length scales ($l_\Omega = \langle\overline{\epsilon'}\rangle^{1/2}/\Omega^{3/2}$) as vertical dotted lines.

	F (Hz)	a	b	R^2
Rectangular blades	2	0.653	-2.5×10^{-3}	1.0000
Rectangular blades	3	0.648	-8.8×10^{-4}	0.9999
Fractal blades	2	0.659	-8.3×10^{-4}	1.0000
Fractal blades	2.5	0.673	-8.3×10^{-4}	1.0000

Table 3. Linear interpolation results of $\langle\overline{\delta u_x'^2}\rangle$ in the r_x direction in the form $ar_x + b$ for the configurations without baffles. The interpolation is done between the Taylor scale λ and the largest scale measured. Here R^2 is the coefficient of determination.

average of the ratio $\overline{(\delta u_x')^2}/\sqrt{\overline{\epsilon'}F}$ instead of the ratio of the spatially averaged terms, $\langle\overline{(\delta u_x')^2}\rangle/\sqrt{\langle\overline{\epsilon'}\rangle F}$, in order to take into account the possible non-homogeneous variation of the dissipation over the field of view. This is consistent with the theoretical approach to non-homogeneous turbulence of Chen & Vassilicos (2022) and Beaumard *et al.* (2024) (e.g. see (7.7) in Beaumard *et al.* (2024)). A good collapse across configurations and a dimensionally correct linear dependence on both r_x and r_z are observed (hence the normalisation of r_x and r_z with D, which is the same in all configurations). The linear interpolation results for $\langle\overline{\delta u_x'^2}\rangle$ in the forms $ar_x + b$ and $ar_z + b$ are presented in tables 3 and 4. These linear interpolations are of very good quality given that the R^2 coefficient is larger than 0.9990 for all configurations. The relative variation of the proportionality coefficient a is relatively small: less than 4 % in the r_x direction and less than 7 % in the r_z direction.

This differs from the baffled configurations studied in Beaumard *et al.* (2024), where power-law behaviours $r_x^{2/3}$ and $r_y^{2/3}$ were found and justified theoretically with a theory initially introduced by Chen & Vassilicos (2022). However, our finding concerning $\overline{\langle(\delta u_x')^2\rangle}/\sqrt{\overline{\epsilon'}F}\rangle$ in rotating non-homogeneous turbulence is very similar to the scaling (1.1) for rotating homogeneous turbulence both because it has the same dependence on Ω and the turbulence dissipation rate and because k^{-2} is equivalent to a linear dependence on the

	F (Hz)	a	b	R^2
Rectangular blades	2	0.591	-2.6×10^{-3}	0.9996
Rectangular blades	3	0.570	-9.0×10^{-4}	0.9990
Fractal blades	2	0.553	1.3×10^{-3}	0.9998
Fractal blades	2.5	0.581	1.3×10^{-3}	0.9996

Table 4. Linear interpolation results of $\langle \overline{\delta u_x'^2} \rangle$ in the r_z direction in the form $ar_z + b$ for the configurations without baffles. The interpolation is done between the Taylor scale λ and the largest scale measured. Here R^2 is the coefficient of determination.

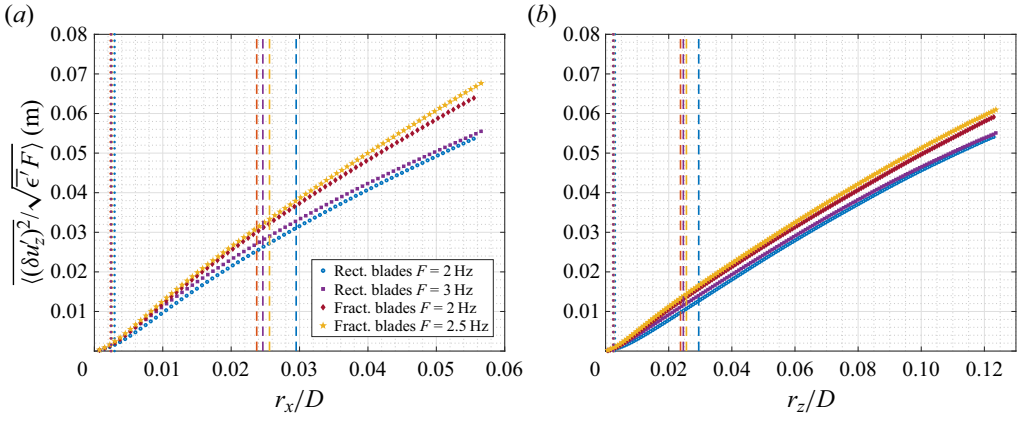

Figure 5. Normalised structure function $\langle \overline{(\delta u_z')^2}/\sqrt{\overline{\epsilon'}F} \rangle$ space-averaged over the field of view versus (*a*) r_x (for $r_z = 0$) and (*b*) r_z (for $r_x = 0$). The units on the vertical axes are metres (m). The Taylor length scales of the different configurations are plotted as vertical dashed lines and the Zeman length scales ($\widetilde{l_\Omega} = \langle \overline{\epsilon'} \rangle^{1/2}/\Omega^{3/2}$) as vertical dotted lines.

two-point separation distance. In agreement with the expectation at the end of the previous section, this is a non-Kolmogorov scaling evidencing a strong and well-defined impact of rotation on the second-order structure function of the horizontal fluctuating velocity component as a function of both r_x and r_z. This is also a scaling that is clearly different from helicity cascade scalings such as the one mentioned in the introduction (see Brissaud *et al.* 1973; Nazarenko & Laval 2000; Herbert *et al.* 2012) because it depends on F and the turbulence dissipation rate.

The plots of $\langle \overline{(\delta u_z')^2}/\overline{\epsilon'}^{1/2} \rangle F^{-1/2}$ in figure 5 do not show good collapse of the fractal and the rectangular blade results. Moreover, the dependencies on r_x and r_z deviate from linear (particularly for the rectangular blades), in agreement with the lack of collapse. Either one or both of F and the turbulence dissipation rate are not involved in the actual scaling of the vertical fluctuating velocity component's second-order structure function or they both are and one additional parameter is needed in the scaling which somehow takes into account differences in the flows generated by fractal and rectangular blade impellers. This is a problem which may require more experiments and which we leave for future research. We did check, however, that the vertical fluctuating velocity component's second-order structure function does not collapse with Kolmogorov scaling and that non-dimensionalisation with D^2F^2 as in Herbert *et al.* (2012) rather than with the square roots of the turbulence dissipation and F does not collapse the rectangular and fractal

blade results for both $\langle\overline{(\delta u_x')^2}\rangle$ and $\langle\overline{(\delta u_z')^2}\rangle$. This observation suggests that the turbulence dissipation rate depends not only on F and D but also on the geometry of the impeller blades. This is visible in our experiments because of our ability to modify the turbulence dissipation rate by changing the blade geometry without changing the rotation speed and the blade frontal area.

Predictions and observations of anisotropic scalings of energy spectra have been made for rapidly rotating homogeneous turbulence (e.g. Galtier 2003; Bellet *et al.* 2006; Thiele & Müller 2009). However, even though the scalings of the horizontal fluctuating velocity's structure function are similar in our rotating non-homogeneous turbulence to scalings claimed for rotating homogeneous turbulence (i.e. proportional to $\sqrt{\Omega}$, the square root of turbulence dissipation and the two-point separation distance), the anisotropy between the scalings of the horizontal and the vertical fluctuating velocity structure functions in our rotating non-homogeneous turbulence bears little resemblance to the spectral anisotropies in rotating homogeneous turbulence. This is an issue which merits future research.

5. Quantification of the different terms of the energy equation

In this section we address the question of the depletion of nonlinearity in rotating non-homogeneous turbulence.

5.1. *Kármán–Howarth–Monin–Hill equation*

Nonlinearity is responsible for interscale turbulent energy transfers. In the presence of all other coexisting turbulence transfer/transport mechanisms, interscale transfers can be studied in terms of two-point equations derived exactly from the incompressible Navier–Stokes equations (see Hill 2001, 2002) without any hypotheses or assumptions, in particular no assumptions of homogeneity.

The incompressible Navier–Stokes equation is written at two points $\boldsymbol{\zeta}^- = \boldsymbol{X} - \boldsymbol{r}$ and $\boldsymbol{\zeta}^+ = \boldsymbol{X} + \boldsymbol{r}$ in physical space, where $\boldsymbol{X}$ is the centroid and $2\boldsymbol{r}$ is the two-point separation vector already introduced in the previous section. One defines the two-point velocity half-difference $\boldsymbol{\delta u}(\boldsymbol{X}, \boldsymbol{r}, t) \equiv (\boldsymbol{u}^+ - \boldsymbol{u}^-)/2$ and half-sum $\boldsymbol{u}_{\boldsymbol{X}}(\boldsymbol{X}, \boldsymbol{r}, t) \equiv (\boldsymbol{u}^+ + \boldsymbol{u}^-)/2$, where $\boldsymbol{u}^+ \equiv \boldsymbol{u}(\boldsymbol{\zeta}^+)$ and $\boldsymbol{u}^- \equiv \boldsymbol{u}(\boldsymbol{\zeta}^-)$ are the fluid velocities at each of the two points, and the two-point pressure half-difference $\delta p(\boldsymbol{X}, \boldsymbol{r}, t) \equiv (p^+ - p^-)/2$, where $p^+ \equiv p(\boldsymbol{\zeta}^+)$ and $p^- \equiv p(\boldsymbol{\zeta}^-)$ are the pressure-to-density ratios at each of the two points. With a Reynolds decomposition into average plus fluctuating quantities, $\boldsymbol{\delta u} = \overline{\boldsymbol{\delta u}} + \boldsymbol{\delta u}'$, $\boldsymbol{u}_{\boldsymbol{X}} = \overline{\boldsymbol{u}_{\boldsymbol{X}}} + \boldsymbol{u}_{\boldsymbol{X}}{}'$ and $\delta p = \delta\bar{p} + \delta p'$, where the overline signifies an average over time, the Navier–Stokes equation implies the following KHMH equation (Hill 2001, 2002; Alves Portela, Papadakis & Vassilicos 2017; Beaumard *et al.* 2024) under the assumption of statistical stationarity, which applies to our constantly agitated turbulent flow:

$$
\begin{aligned}
&(\overline{\boldsymbol{u}_{\boldsymbol{X}}}\cdot\boldsymbol{\nabla}_{\boldsymbol{X}} + \boldsymbol{\delta}\bar{\boldsymbol{u}}\cdot\boldsymbol{\nabla}_{\boldsymbol{r}})\,\frac{1}{2}\overline{|\boldsymbol{\delta u}'|^2} - P_r - P^s_{Xr} + \boldsymbol{\nabla}_{\boldsymbol{X}}\cdot\left(\overline{\boldsymbol{u}_{\boldsymbol{X}}{}'\frac{1}{2}|\boldsymbol{\delta u}'|^2}\right) + \boldsymbol{\nabla}_{\boldsymbol{r}}\cdot\left(\overline{\boldsymbol{\delta u}'\frac{1}{2}|\boldsymbol{\delta u}'|^2}\right)\\
&\quad= -\boldsymbol{\nabla}_{\boldsymbol{X}}\cdot\overline{(\boldsymbol{\delta u}'\delta p')} + \frac{\nu}{2}\boldsymbol{\nabla}_{\boldsymbol{X}}{}^2\frac{1}{2}\overline{|\boldsymbol{\delta u}'|^2} + \frac{\nu}{2}\boldsymbol{\nabla}_{\boldsymbol{r}}{}^2\frac{1}{2}\overline{|\boldsymbol{\delta u}'|^2} - \frac{\nu}{4}\overline{\frac{\partial u_i'^+}{\partial\zeta_k^+}\frac{\partial u_i'^+}{\partial\zeta_k^+}}\\
&\qquad- \frac{\nu}{4}\overline{\frac{\partial u_i'^-}{\partial\zeta_k^-}\frac{\partial u_i'^-}{\partial\zeta_k^-}},
\end{aligned}
\tag{5.1}
$$

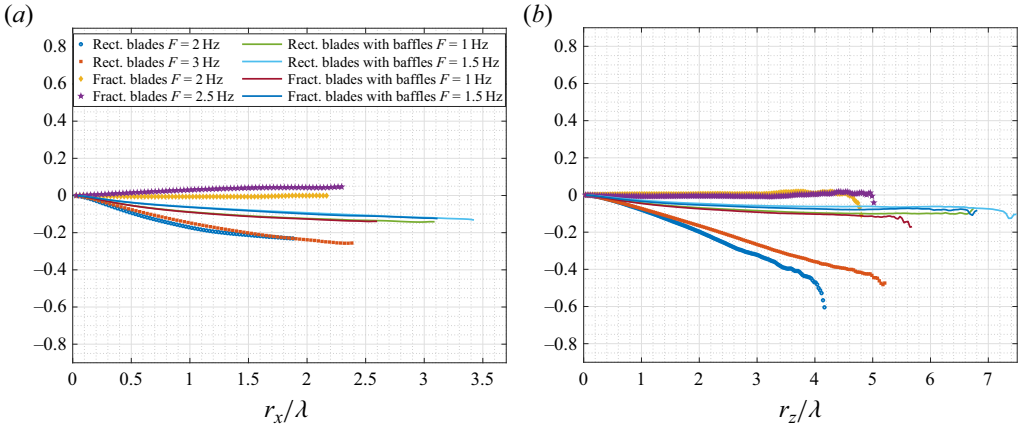

Figure 6. Normalised truncation estimate of the total two-point turbulence production rate $2\langle\widetilde{P}_r + \widetilde{P^s_{Xr}}\rangle/\langle\overline{\epsilon'}\rangle$ versus (*a*) r_x/λ (for $r_z = 0$) and (*b*) r_z/λ (for $r_x = 0$).

where $P_r = -\overline{\delta u'_j \delta u'_i}(\partial \delta\overline{u_i}/\partial r_j)$ and $P^s_{Xr} = -\overline{u'_{Xj}\delta u'_i}(\partial\delta\overline{u_i}/\partial X_j)$ are small-scale two-point turbulence production rates (see Beaumard *et al.* 2024).

5.2. *Two-point turbulence production rates*

We start our data analysis with an assessment of the two-point turbulence production rates. The sums defining $P_r = -\overline{\delta u'_j \delta u'_i}(\partial\delta\overline{u_i}/\partial r_j)$ and $P^s_{Xr} = -\overline{u'_{Xj}\delta u'_i}(\partial\delta\overline{u_i}/\partial X_j)$ are sums of nine terms, of which our 2D2C PIV has access to only four. Our data therefore allow only truncations to be calculated directly. The accessible truncation of P_r is

$$\widetilde{P}_r = -\overline{\delta u'_x \delta u'_x}\frac{\partial\delta\overline{u_x}}{\partial r_x} - \overline{\delta u'_x \delta u'_z}\frac{\partial\delta\overline{u_z}}{\partial r_x} - \overline{\delta u'_z \delta u'_x}\frac{\partial\delta\overline{u_x}}{\partial r_z} - \overline{\delta u'_z \delta u'_z}\frac{\partial\delta\overline{u_z}}{\partial r_z}, \tag{5.2}$$

with

$$\overline{\delta u'_y \delta u'_y}\frac{\partial\delta\overline{u_y}}{\partial r_y} + \overline{\delta u'_x \delta u'_y}\frac{\partial\delta\overline{u_y}}{\partial r_x} + \overline{\delta u'_x \delta u'_y}\frac{\partial\delta\overline{u_x}}{\partial r_y} + \overline{\delta u'_z \delta u'_y}\frac{\partial\delta\overline{u_y}}{\partial r_z} + \overline{\delta u'_z \delta u'_y}\frac{\partial\delta\overline{u_z}}{\partial r_y} \tag{5.3}$$

being the difference between $\widetilde{P}_r$ and P_r. Similarly, we have the following truncation estimate of P^s_{Xr}:

$$\widetilde{P^s_{Xr}} = -\overline{u'_{Xx}\delta u'_x}\frac{\partial\delta\overline{u_x}}{\partial X_x} - \overline{u'_{Xx}\delta u'_z}\frac{\partial\delta\overline{u_z}}{\partial X_x} - \overline{u'_{Xz}\delta u'_x}\frac{\partial\delta\overline{u_x}}{\partial X_z} - \overline{u'_{Xz}\delta u'_z}\frac{\partial\delta\overline{u_z}}{\partial X_z}. \tag{5.4}$$

Our conclusions for the full two-point turbulence production rates are of course contingent on how closely the truncation estimates capture their behaviour. Even so, our results provide definite insights into the non-homogeneity of the flow and the resulting production physics. We calculate space averages over the field of view of the two truncated two-point production rates ($\langle\widetilde{P}_r\rangle$ and $\langle\widetilde{P^s_{Xr}}\rangle$) and we plot their sum, normalised by $\langle\overline{\epsilon'}\rangle/2$, in figure 6 versus r_x and r_z.

For all four baffled configurations, the values of $(\langle\widetilde{P}_r\rangle + \langle\widetilde{P^s_{Xr}}\rangle)/\langle\overline{\epsilon'}\rangle$ collapse and are relatively small for most values of r_x and r_z to which our field of view allows access. Whilst $\langle\widetilde{P}_r\rangle + \langle\widetilde{P^s_{Xr}}\rangle$ is negligible at all accessible scales for the unbaffled fractal blade configurations, it is definitely very significant as a fraction of the turbulence dissipation

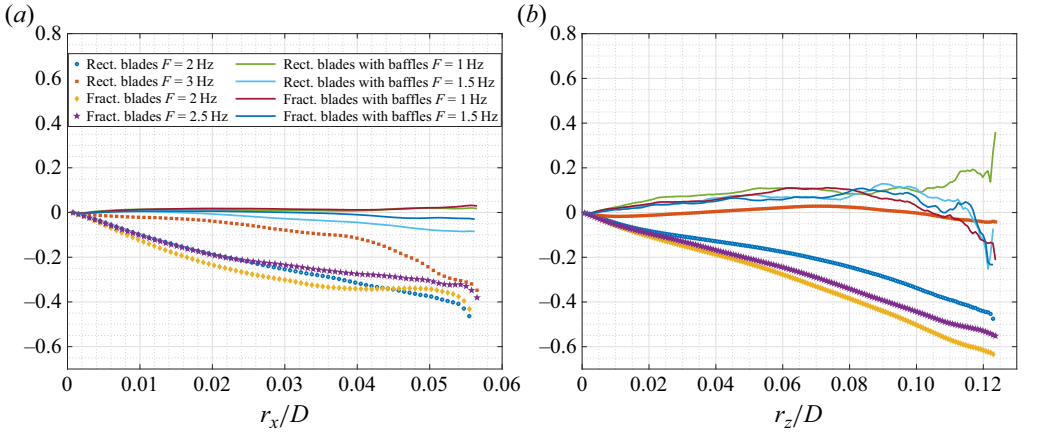

Figure 7. Normalised truncation estimate of the linear spatial transport rate $2\langle\overline{\boldsymbol{u_X}}\cdot\widetilde{\boldsymbol{\nabla}_X\tfrac{1}{2}|\boldsymbol{\delta u'}|^2}\rangle/\langle\overline{\epsilon'}\rangle$ versus (*a*) r_x/D (for $r_z = 0$) and (*b*) r_z/D (for $r_x = 0$).

rate for the unbaffled rectangular blade configurations at all scales larger than λ. This stark non-homogeneity difference between rectangular and fractal blades, perhaps resulting from the fractal blades' breaking of large-scale coherent structures (Başbuğ, Papadakis & Vassilicos 2018), makes the collapse of the horizontal fluctuating velocity structure functions in figure 4 for all unbaffled configurations all the more remarkable. Even if small-scale turbulence production is negligible in the unbaffled fractal configurations, the turbulence in these configurations is nevertheless non-homogeneous as seen in the remainder of § 5.

5.3. *Small-scale linear transport*

We now focus on another term of the KHMH equation: the linear spatial transport rate $\overline{\boldsymbol{u_X}}\cdot\boldsymbol{\nabla}_X\frac{1}{2}\overline{|\boldsymbol{\delta u'}|^2}$, which is also a term reflecting turbulence non-homogeneity. A non-zero linear spatial transport rate means that two-point turbulent energy ($\frac{1}{2}\overline{|\boldsymbol{\delta u'}|^2}$) enters or leaves the domain with the mean flow. Our 2D2C PIV data allow us to calculate the following truncated estimate of this term: $\langle\widetilde{\overline{\boldsymbol{u_X}}\cdot\boldsymbol{\nabla}_X\frac{1}{2}\overline{|\boldsymbol{\delta u'}|^2}}\rangle \equiv \langle(\overline{u_{Xx}}(\partial/\partial X_x) + \overline{u_{Xz}}(\partial/\partial X_z))\frac{1}{2}(\overline{\delta u_x'^2 + \delta u_z'^2})\rangle$. In figure 7, we plot this estimate normalised by $\langle\overline{\epsilon'}\rangle/2$ versus r_x and r_z. It appears small compared with $\langle\overline{\epsilon'}\rangle/2$ for all accessible r_x and r_z in all baffled configurations. However, it is not so small compared with $\langle\overline{\epsilon'}\rangle/2$ for most accessible r_x and r_z above λ in all unbaffled configurations except the one with rectangular blades and $F = 3$ Hz.

All in all, the non-homogeneity generated by rectangular blades is characterised by a significant two-point turbulence production rate and, depending on F, a significant or small two-point linear spatial transport rate. By contrast, the non-homogeneity generated by fractal blades is characterised by a significant two-point linear spatial transport rate but a negligible two-point turbulent production rate. The non-homogeneities generated by these two different types of blade are qualitatively different.

5.4. *Energy transfer rate measurements*

Given the differences between the structure functions $\langle\overline{\delta u_x'^2}\rangle$ and $\langle\overline{\delta u_z'^2}\rangle$ reported in § 4, we now look at energy transfer rates separately for each of these two structure functions.

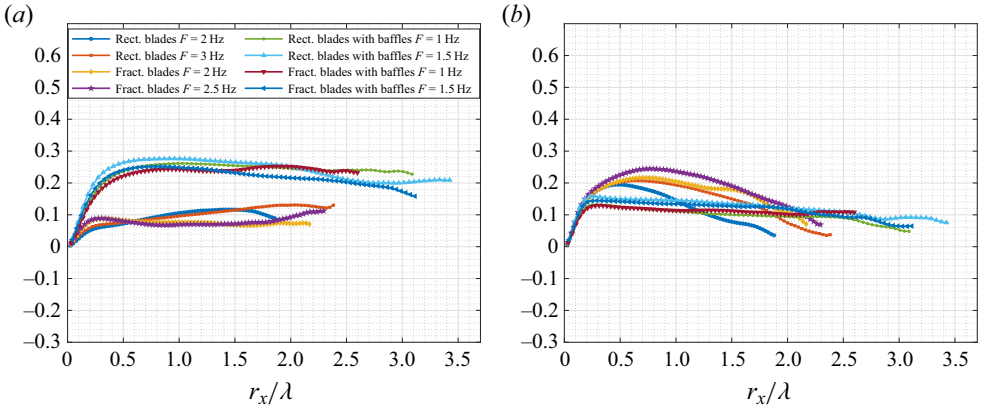

Figure 8. Space- and time-averaged truncation estimates of the small-scale interscale transfer of the energy contributions $\delta u_x'^2$ and $\delta u_z'^2$ normalised by dissipation and along the r_x direction: (*a*) $-\langle \nabla_{\boldsymbol{r}} \cdot (\widetilde{\boldsymbol{\delta u}' \tfrac{1}{2}\delta u_x'^2}) \rangle / \langle \tfrac{1}{2}\overline{\epsilon'} \rangle$; (*b*) $-\langle \nabla_{\boldsymbol{r}} \cdot (\widetilde{\boldsymbol{\delta u}' \tfrac{1}{2}\delta u_z'^2}) \rangle / \langle \tfrac{1}{2}\overline{\epsilon'} \rangle$. Here $r_z = 0$.

The KHMH equation (5.1) is the sum over index i of the following three equations (one equation per index $i = 1, 2, 3$):

$$\begin{aligned}
&(\overline{\boldsymbol{u}_{\boldsymbol{X}}} \cdot \nabla_{\boldsymbol{X}} + \boldsymbol{\delta \bar{u}} \cdot \nabla_{\boldsymbol{r}}) \frac{1}{2}\overline{\delta u_i'^2} + \overline{\delta u_j' \delta u_i'} \frac{\partial \delta \overline{u_i}}{\partial r_j} + \overline{u_{Xj}' \delta u_i'} \frac{\partial \delta \overline{u_i}}{\partial X_j} \\
&\quad + \nabla_{\boldsymbol{X}} \cdot \left(\overline{\boldsymbol{u}_{\boldsymbol{X}}' \frac{1}{2}\delta u_i'^2} \right) + \nabla_{\boldsymbol{r}} \cdot \left(\overline{\boldsymbol{\delta u}' \frac{1}{2}\delta u_i'^2} \right) \\
&= -\overline{\delta u_i' \frac{\partial \delta p'}{\partial X_i}} + \frac{\nu}{2} \nabla_{\boldsymbol{X}}{}^2 \frac{1}{2}\overline{\delta u_i'^2} + \frac{\nu}{2} \nabla_{\boldsymbol{r}}{}^2 \frac{1}{2}\overline{\delta u_i'^2} - \frac{\nu}{4} \overline{\frac{\partial u_i'^+}{\partial \zeta_k^+} \frac{\partial u_i'^+}{\partial \zeta_k^+}} - \frac{\nu}{4} \overline{\frac{\partial u_i'^-}{\partial \zeta_k^-} \frac{\partial u_i'^-}{\partial \zeta_k^-}},
\end{aligned} \tag{5.5}$$

with implicit summations over j and over k but not over i. These three equations, one per index i, hold in them the interscale and interspace transfer rates of two-point turbulent energy in the fluctuating velocity component indexed by i. We concentrate on $i = 1$ for $\delta u_x'^2$ and $i = 3$ for $\delta u_z'^2$.

The limitations of our 2D2C PIV allow us to access truncated estimates of the interscale and interspace transfer rates. In figures 8 and 9, we plot the normalised truncated interscale transfer rates

$$\left\langle \nabla_{\boldsymbol{r}} \cdot \left(\widetilde{\boldsymbol{\delta u}' \frac{1}{2}\delta u_x'^2} \right) \right\rangle \Big/ \left\langle \frac{1}{2}\overline{\epsilon'} \right\rangle \equiv \left\langle \overline{\delta u_x' \frac{\partial}{\partial r_x} \frac{1}{2}\delta u_x'^2} \right\rangle \Big/ \left\langle \frac{1}{2}\overline{\epsilon'} \right\rangle + \left\langle \overline{\delta u_z' \frac{\partial}{\partial r_z} \frac{1}{2}\delta u_x'^2} \right\rangle \Big/ \left\langle \frac{1}{2}\overline{\epsilon'} \right\rangle \tag{5.6}$$

and

$$\left\langle \nabla_{\boldsymbol{r}} \cdot \left(\widetilde{\boldsymbol{\delta u}' \frac{1}{2}\delta u_z'^2} \right) \right\rangle \Big/ \left\langle \frac{1}{2}\overline{\epsilon'} \right\rangle \equiv \left\langle \overline{\delta u_x' \frac{\partial}{\partial r_x} \frac{1}{2}\delta u_z'^2} \right\rangle \Big/ \left\langle \frac{1}{2}\overline{\epsilon'} \right\rangle + \left\langle \overline{\delta u_z' \frac{\partial}{\partial r_z} \frac{1}{2}\delta u_z'^2} \right\rangle \Big/ \left\langle \frac{1}{2}\overline{\epsilon'} \right\rangle. \tag{5.7}$$

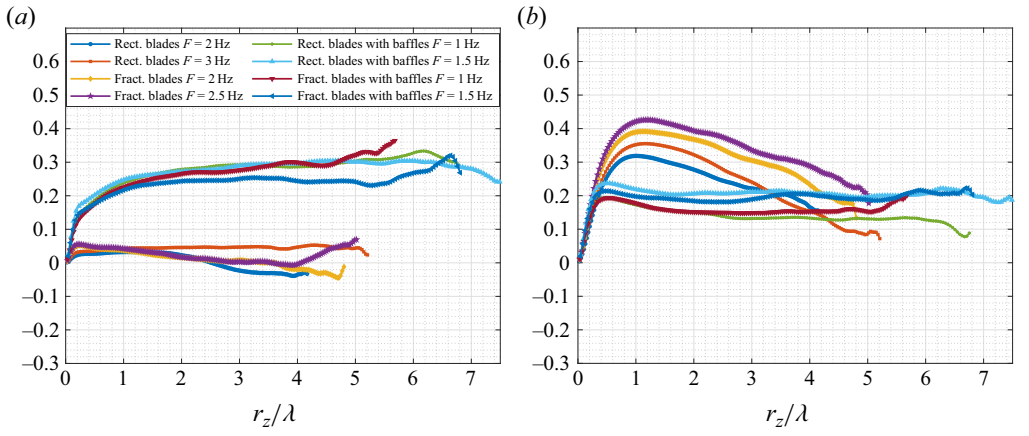

Figure 9. Space- and time-averaged truncation estimates of the small-scale interscale transfer of the energy contributions $\delta u_x'^2$ and $\delta u_z'^2$ normalised by dissipation and along the r_z direction: (*a*) $-\langle \nabla_{\boldsymbol{r}} \cdot (\widetilde{\boldsymbol{\delta u}' \overline{\frac{1}{2}\delta u_x'^2}}) \rangle / \langle \overline{\frac{1}{2}\epsilon'} \rangle$; (*b*) $-\langle \nabla_{\boldsymbol{r}} \cdot (\widetilde{\boldsymbol{\delta u}' \overline{\frac{1}{2}\delta u_z'^2}}) \rangle / \langle \overline{\frac{1}{2}\epsilon'} \rangle$. Here $r_x = 0$.

Similarly, we plot in figures 10 and 11 the normalised truncated interspace transfer rates

$$\left\langle \nabla_{\boldsymbol{X}} \cdot \left(\widetilde{\boldsymbol{u}_{\boldsymbol{X}}' \overline{\frac{1}{2}\delta u_x'^2}} \right) \right\rangle \Big/ \left\langle \overline{\frac{1}{2}\epsilon'} \right\rangle \equiv \left\langle \overline{u_{Xx}' \frac{\partial}{\partial X_x} \frac{1}{2}\delta u_x'^2} \right\rangle \Big/ \left\langle \overline{\frac{1}{2}\epsilon'} \right\rangle + \left\langle \overline{u_{Xz}' \frac{\partial}{\partial X_z} \frac{1}{2}\delta u_x'^2} \right\rangle \Big/ \left\langle \overline{\frac{1}{2}\epsilon'} \right\rangle \tag{5.8}$$

and

$$\left\langle \nabla_{\boldsymbol{X}} \cdot \left(\widetilde{\boldsymbol{u}_{\boldsymbol{X}}' \overline{\frac{1}{2}\delta u_z'^2}} \right) \right\rangle \Big/ \left\langle \overline{\frac{1}{2}\epsilon'} \right\rangle \equiv \left\langle \overline{u_{Xx}' \frac{\partial}{\partial X_x} \frac{1}{2}\delta u_z'^2} \right\rangle \Big/ \left\langle \overline{\frac{1}{2}\epsilon'} \right\rangle + \left\langle \overline{u_{Xz}' \frac{\partial}{\partial X_z} \frac{1}{2}\delta u_z'^2} \right\rangle \Big/ \left\langle \overline{\frac{1}{2}\epsilon'} \right\rangle. \tag{5.9}$$

We first comment on figures 8 and 9. Our $\delta u_x'^2$ interscale transfer rate estimates (see figures 8*a* and 9*a*) suggest that rotation in the unbaffled configurations causes a depletion in the r_x direction and a near-suppression in the r_z direction of interscale transfer nonlinearity (note that depletion of the interscale energy transfer rate does not necessarily indicate depletion of nonlinearity as in the enstrophy transfer range of periodic/homogeneous two-dimensional turbulence, where average interscale energy transfers vanish). With the exception of this near-suppression where $\langle \nabla_{\boldsymbol{r}} \cdot (\widetilde{\boldsymbol{\delta u}' \overline{\frac{1}{2}\delta u_x'^2}}) \rangle / \langle \overline{\frac{1}{2}\epsilon'} \rangle$ is close to zero for all accessible values of r_z when $r_x = 0$, all our truncation estimates of interscale transfer rates in figures 8 and 9 are negative, suggesting interscale turbulent energy transfers from large to small scales irrespective of configuration. However, whereas the results for the baffled configurations seem to collapse with the normalisation by the turbulence dissipation rate as functions of both r_x/λ and r_z/λ and even be approximately constant for r_x and r_z larger than λ or a fraction of λ (see also Beaumard *et al.* 2024), for the unbaffled configurations this is only the case for the $\delta u_x'^2$ and not the $\delta u_z'^2$ interscale transfer rates. In fact, the $\delta u_z'^2$ interscale transfer rate (see figures 8*b* and 9*b*) not only loses its collapsing scaling with turbulence dissipation rate in the presence of rotation (unbaffled configurations) but also appears intensified by rotation

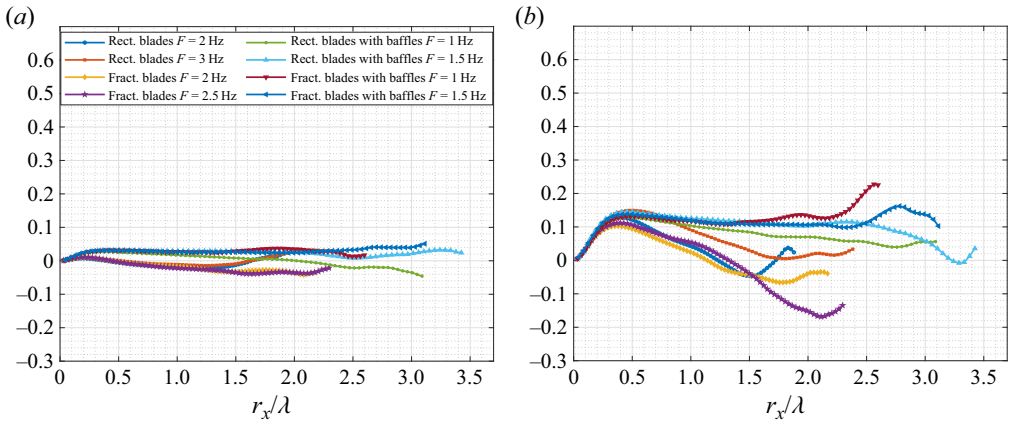

Figure 10. Space- and time-averaged truncation estimates of the small-scale interspace transfer of the energy contributions $\delta u_x'^2$ and $\delta u_z'^2$ normalised by dissipation and along the r_x direction: (*a*) $\langle \nabla_{\boldsymbol{X}} \cdot \widetilde{(\boldsymbol{u}_{\boldsymbol{X}}' \frac{1}{2}\delta u_x'^2)} \rangle / \langle \frac{1}{2}\overline{\epsilon'} \rangle$; (*b*) $\langle \nabla_{\boldsymbol{X}} \cdot \widetilde{(\boldsymbol{u}_{\boldsymbol{X}}' \frac{1}{2}\delta u_z'^2)} \rangle / \langle \frac{1}{2}\overline{\epsilon'} \rangle$. Here $r_z = 0$.

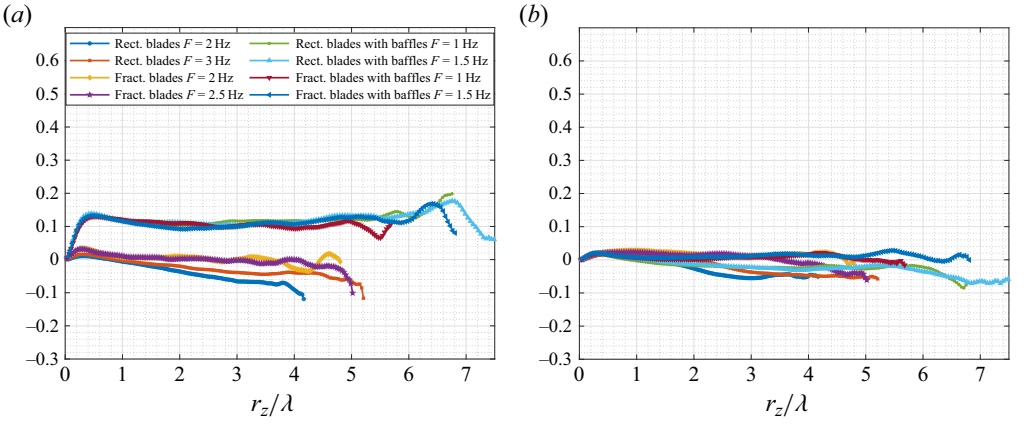

Figure 11. Space- and time-averaged truncation estimates of the small-scale interspace transfer of the energy contributions $\delta u_x'^2$ and $\delta u_z'^2$ normalised by dissipation and along the r_z direction: (*a*) $\langle \nabla_{\boldsymbol{X}} \cdot \widetilde{(\boldsymbol{u}_{\boldsymbol{X}}' \frac{1}{2}\delta u_x'^2)} \rangle / \langle \frac{1}{2}\overline{\epsilon'} \rangle$; (*b*) $\langle \nabla_{\boldsymbol{X}} \cdot \widetilde{(\boldsymbol{u}_{\boldsymbol{X}}' \frac{1}{2}\delta u_z'^2)} \rangle / \langle \frac{1}{2}\overline{\epsilon'} \rangle$. Here $r_x = 0$.

over a range of r_x and r_z scales, particularly around λ, and decreases with increasing r_z above λ. In other words, rotation intensifies interscale transfer nonlinearity as far as $\delta u_z'^2$ is concerned and also makes it dependent on r_x and r_z. Our results are based on the measured contributions and may not represent the full energy transfers. However, the observed qualitative differences in these contributions between baffled and non-baffled contributions are significant in themselves and demonstrate a clear impact of the flow rotation on interscale turbulent energy transfer rates.

These qualitative differences between $\langle \nabla_{\boldsymbol{r}} \cdot \widetilde{(\boldsymbol{\delta u}' \frac{1}{2}\delta u_x'^2)} \rangle / \langle \frac{1}{2}\overline{\epsilon'} \rangle$ and $\langle \nabla_{\boldsymbol{r}} \cdot \widetilde{(\boldsymbol{\delta u}' \frac{1}{2}\delta u_z'^2)} \rangle / \langle \frac{1}{2}\overline{\epsilon'} \rangle$ in the unbaffled configurations echo the fact that there are also differences between the scalings of $\overline{\delta u_x'^2}$ and $\overline{\delta u_z'^2}$ in these configurations as reported in § 4.

Interestingly, if the arguments of Kraichnan (1965) and Zhou (1995) could be translated to low-Rossby-number rotating non-homogeneous turbulence (unbaffled configurations), even though they were developed for low-Rossby-number rotating homogeneous turbulence, it might be possible to claim that $\langle \nabla_{\boldsymbol{r}} \cdot (\widetilde{\overline{\boldsymbol{\delta u}' \tfrac{1}{2} \delta u_x'^2}}) \rangle$ is a function of only the time scale Ω^{-1} and a turbulent energy density $(\mathrm{d}/\mathrm{d}r_x)\langle \overline{\delta u_x'^2} \rangle$. Such a claim would act as a bridge between the results in figure 4(*a*) and the unbaffled results in figure 8(*a*) because $\langle \overline{\delta u_x'^2} \rangle \sim r_x \sqrt{\langle \overline{\epsilon'} \rangle \Omega}$ (effectively figure 4*a*) would then imply that $\langle \nabla_{\boldsymbol{r}} \cdot (\widetilde{\overline{\boldsymbol{\delta u}' \tfrac{1}{2} \delta u_x'^2}}) \rangle / \langle \overline{\tfrac{1}{2} \epsilon'} \rangle$ is a constant independent of Ω, r_x and impeller blade as figure 8(*a*) might indeed suggest. It is not clear, though, if and why such an argument might work for the r_x dependence of $\langle \nabla_{\boldsymbol{r}} \cdot (\widetilde{\overline{\boldsymbol{\delta u}' \tfrac{1}{2} \delta u_x'^2}}) \rangle$ and perhaps not for its r_z dependence.

We now comment on figures 10 and 11. Firstly, our truncation estimates of the interspace transport rates of $\delta u_x'^2$ for $r_z = 0$ and $r_x \neq 0$ and of $\delta u_z'^2$ for $r_x = 0$ and $r_z \neq 0$ appear small for all configurations, both baffled and unbaffled. The comparison of baffled and unbaffled results in figure 11(*a*) suggests a severe depletion by rotation of the nonlinearity that controls the interspace transport of $\delta u_x'^2$ for $r_x = 0$ and any accessible r_z. In fact, the rotation seems to lead to near-suppression of the interspace transport of $\delta u_x'^2$ in the fractal blade configurations but may be forcing the interspace transport of $\delta u_x'^2$ to change sign in the rectangular blade configurations at the larger values of r_z (see figure 11*a*). As already documented earlier in this paper, the non-homogeneity structures of rectangular and fractal blade configurations are different, and this seems to be another difference in their non-homogeneities.

The interspace transport rates in figures 10(*b*) and 11(*a*) for the baffled configurations are positive and seem to more or less collapse with turbulence dissipation rate within a range of scales larger than 0.5λ where the interspace transport rates are about constant. This behaviour has been explained by Beaumard *et al.* (2024) on the basis of the theory of Chen & Vassilicos (2022) and is not the focus of the present work. Here we note that rotation severely modifies this interspace transport behaviour by effectively suppressing the measured contributions to the interspace transport of $\delta u_x'^2$, as already mentioned in the previous paragraph, and by changing the dependence on r_x of the measured contributions to the interspace transport rate of $\delta u_z'^2$ (see figure 10*b*). The change of behaviour of the measured interspace transport contributions may or may not reflect the behaviour of the full interspace transport rate. However, a clear change compared with the baffled configuration is evidently clear.

6. Conclusion

Time-resolved PIV measurements have been carried out in a mixing tank stirred by a rotating impeller without baffles generating a rotating turbulent flow in the field of view under the impeller. This flow has been compared with the flow generated at the same position in the presence of baffles which break the rotation. The Zeman length is much smaller than the Taylor length in the unbaffled experiments, suggesting a strong impact of rotation over all accessible length scales. The horizontal fluctuating velocity's second-order structure function is found to be proportional to the two-point separation distance and to the square root of the rotation speed and of the turbulence dissipation rate, similarly to expectations for rapidly rotating homogeneous turbulence, even though the rotating turbulence in the present unbaffled experiments is not homogeneous. In fact,

this scaling of the structure function holds with the same non-dimensional coefficient for different rotation speeds and different impeller blades, even though the turbulent flows generated by fractal and rectangular rotating blades have qualitatively very different non-homogeneities (see §§ 5.2 and 5.3, in particular the last paragraph of § 5.3).

The nonlinearity associated with the measured terms of both the interscale and the interspace transfer rates of horizontal turbulence fluctuating energy is found to be severely depleted if not suppressed by the rotation. However, the nonlinearity associated with the measured terms of the interscale and the interspace transfer rates of vertical turbulence fluctuating energy (in the direction of the axis of rotation) is, to the contrary, enhanced and/or modified by rotation as a function of the two-point separation distance and in terms of scalings (see § 5.4).

This difference between horizontal and vertical nonlinearities is accompanied by a difference between the horizontal and the vertical fluctuating velocity's second-order structure functions. The vertical fluctuating velocity's second-order structure function does not scale like the horizontal one and does not follow Kolmogorov scalings either.

Acknowledgements. The CNRS Research Federation on Ground Transports and Mobility, in articulation with the Elsat2020 project supported by the European Community, the French Ministry of Higher Education and Research and the Hauts de France Regional Council are acknowledged for the funding of the PIV equipment used in this study.

Funding. This work was directly supported by J.C.V.'s Chair of Excellence CoPreFlo funded by I-SITE-ULNE (grant number R-TALENT-19-001-VASSILICOS), MEL (grant number CONVENTION_219_ESR_06) and Region Hauts de France (grant number 20003862), and by ERC Advanced Grant NoStaHo funded by the European Union. Views and opinions expressed are, however, those of the authors only and do not necessarily reflect those of the European Union or the European Research Council. Neither the European Union nor the granting authority can be held responsible for them.

Declaration of interests. The authors report no conflict of interest.

Data availability statement. The data that support the findings of this study are available upon request.

Author ORCIDs.
P. Beaumard https://orcid.org/0009-0003-6654-1854;
P. Bragança https://orcid.org/0009-0005-5290-1913;
C. Cuvier https://orcid.org/0000-0001-6108-6942;
J.C. Vassilicos https://orcid.org/0000-0003-1828-6628.

Appendix. Turbulent kinetic energy spatial distribution

Distributions of the measured turbulent kinetic energy in space are presented for one non-baffled and one baffled configuration in figure 12(*a*,*b*). The statistics are converged with 50 000 velocity fields (one velocity field per packet as opposed to the other results of the publication; see more details in § 2). The spatial variation is only around 3 % for the non-baffled configuration and around 4 % for the baffled configuration. For both configurations, the shapes of the non-homogeneous distributions of the turbulent kinetic energy are consistent with the spatial variations of the mean flow identified in figure 3(*a*,*b*) with a non-homogeneity mainly in the vertical direction. For the non-baffled configuration, the minor variation observed in figure 3(*a*) for the mean flow in the horizontal direction is also visible and even more pronounced for the turbulent kinetic energy in figure 12(*a*). For the baffled configuration, the variation of turbulent kinetic energy in figure 12(*b*) is inverted compared with the mean flow variation in figure 3(*b*).

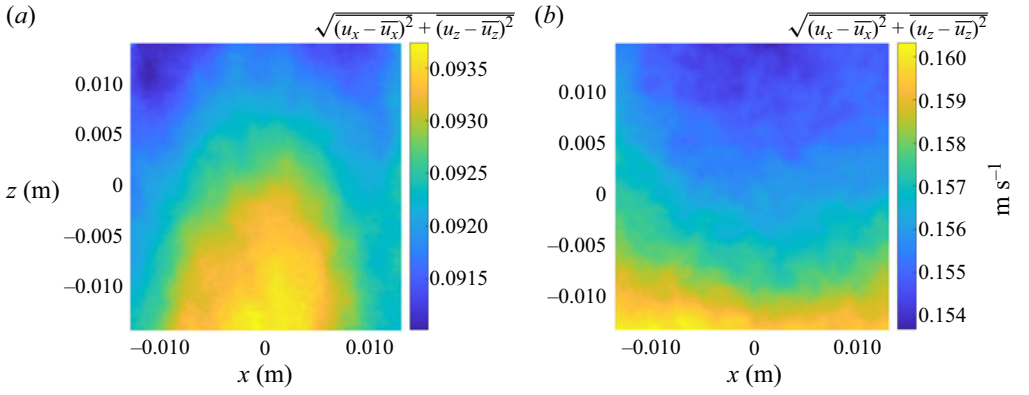

Figure 12. Standard deviation of both velocity components measured within the measurement plane shown in figure 2 of a configuration with rectangular blades and without baffles. (*a*) Rectangular blade without baffles ($F = 3$ Hz). (*b*) Rectangular blade with baffles ($F = 1.5$ Hz).

References

Alves Portela, F., Papadakis, G. & Vassilicos, J.C. 2017 The turbulence cascade in the near wake of a square prism. *J. Fluid Mech.* **825**, 315–352.

Baroud, C.N., Plapp, B.B., She, Z.-S. & Swinney, H.L. 2002 Anomalous self-similarity in a turbulent rapidly rotating fluid. *Phys. Rev. Lett.* **88** (11), 114501.

Batchelor, G.K. 1953 *The Theory of Homogeneous Turbulence*. Cambridge University Press.

Başbuğ, S., Papadakis, G. & Vassilicos, J.C. 2018 Reduced power consumption in stirred vessels by means of fractal impellers. *AIChE J.* **64** (4), 1485–1499.

Beaumard, P., Braganća, P., Cuvier, C., Steiros, K. & Vassilicos, J.C. 2024 Scale-by-scale non-equilibrium with Kolmogorov-like scalings in non-homogeneous stationary turbulence. *J. Fluid Mech.* **984**, A35.

Bellet, F., Godeferd, F.S., Scott, J.F. & Cambon, C. 2006 Wave turbulence in rapidly rotating flows. *J. Fluid Mech.* **562**, 83–121.

Brissaud, A., Frisch, U., Leorat, J., Lesieur, M. & Mazure, A. 1973 Helicity cascades in fully developed isotropic turbulence. *Phys. Fluids* **16** (8), 1366.

Canuto, V.M. & Dubovikov, M.S. 1997 Physical regimes and dimensional structure of rotating turbulence. *Phys. Rev. Lett.* **78** (4), 666–669.

Chen, J.G. & Vassilicos, J.C. 2022 Scalings of scale-by-scale turbulence energy in non-homogeneous turbulence. *J. Fluid Mech.* **938**, A7.

Corrsin, S. 1958 Local isotropy in turbulent shear flow. *Tech. Rep.* RM 58B11. National Advisory Committee for Aeronautics.

Delache, A., Cambon, C. & Godeferd, F. 2014 Scale by scale anisotropy in freely decaying rotating turbulence. *Phys. Fluids* **26** (2), 025104.

Frisch, U. 1995 *Turbulence: The Legacy of A. N. Kolmogorov*. Cambridge University Press.

Galtier, S. 2003 Weak inertial-wave turbulence theory. *Phys. Rev.* E **68** (1), 015301.

Galtier, S. 2009 Exact vectorial law for homogeneous rotating turbulence. *Phys. Rev.* E **80** (4), 046301.

Galtier, S. 2022 *Physics of Wave Turbulence*. Cambridge University Press.

Godeferd, F.S. & Moisy, F. 2015 Structure and dynamics of rotating turbulence: a review of recent experimental and numerical results. *Appl. Mech. Rev.* **67** (3), 030802.

Herbert, E., Daviaud, F., Dubrulle, B., Nazarenko, S. & Naso, A. 2012 Dual non-Kolmogorov cascades in a von Kármán flow. *Europhys. Lett.* **100** (4), 44003.

Hill, R.J. 2001 Equations relating structure functions of all orders. *J. Fluid Mech.* **434**, 379–388.

Hill, R.J. 2002 The approach of turbulence to the locally homogeneous asymptote as studied using exact structure-function equations. arXiv:physics/0206034.

Kolmogorov, A.N. 1941*a* Dissipation of energy in the locally isotropic turbulence. *Dokl. Akad. Nauk SSSR* **32** (1941), 16–18.

Kolmogorov, A.N. 1941*b* The local structure of turbulence in incompressible viscous fluid for very large Reynolds numbers. *Dokl. Akad. Nauk SSSR* **30** (1941), 301–305.

Kraichnan, R.H. 1965 Inertial-range spectrum of hydromagnetic turbulence. *Phys. Fluids* **8** (7), 1385–1387.

MORIZE, C., MOISY, F. & RABAUD, M. 2005 Decaying grid-generated turbulence in a rotating tank. *Phys. Fluids* **17** (9), 095105.

NAGATA, S. 1975 *Mixing: Principles and Applications*. Halsted Press.

NAZARENKO, S. & LAVAL, J.-P. 2000 Non-local two-dimensional turbulence and Batchelor's regime for passive scalars. *J. Fluid Mech.* **408**, 301–321.

OBUKHOV, A.M. 1941 On the distribution of energy in the spectrum of turbulent flow. *Dokl. Akad. Nauk SSSR*. **32**, 19–21.

POPE, S.B. 2000 *Turbulent Flows*. Cambridge University Press.

SAGAUT, P. & CAMBON, C. 2018 *Homogeneous Turbulence Dynamics*. Springer.

STEIROS, K., BRUCE, P.J.K., BUXTON, O.R.H. & VASSILICOS, J.C. 2017*a* Effect of blade modifications on the torque and flow field of radial impellers in stirred tanks. *Phys. Rev. Fluids* **2** (9), 094802.

STEIROS, K., BRUCE, P.J.K., BUXTON, O.R.H. & VASSILICOS, J.C. 2017*b* Power consumption and form drag of regular and fractal-shaped turbines in a stirred tank. *AIChE J.* **63** (2), 843–854.

THIELE, M. & MÜLLER, W.-C. 2009 Structure and decay of rotating homogeneous turbulence. *J. Fluid Mech.* **637**, 425–442.

YEUNG, P.K. & ZHOU, Y. 1998 Numerical study of rotating turbulence with external forcing. *Phys. Fluids* **10** (11), 2895–2909.

ZEMAN, O. 1994 A note on the spectra and decay of rotating homogeneous turbulence. *Phys. Fluids* **6** (10), 3221–3223.

ZHOU, Y. 1995 A phenomenological treatment of rotating turbulence. *Phys. Fluids* **7** (8), 2092–2094.